How is carbonate crust digested by magma?

Anastassia Yu. Borisova, Wendy A Bohrson

frontiers | Frontiers in Earth Science

TYPE Original Research
PUBLISHED 10 August 2023
DOI 10.3389/feart.2023.1186207

OPEN ACCESS

EDITED BY
Patrizia Fiannacca,
University of Catania, Italy

REVIEWED BY
Rong Xu,
Chinese Academy of Sciences (CAS), China
Saskia Erdmann,
UMR7327 Institut des Sciences de la Terre d'Orléans (ISTO), France

*CORRESPONDENCE
Anastassia Y. Borisova,
anastassia.borisova@get.omp.eu

RECEIVED 14 March 2023
ACCEPTED 28 June 2023
PUBLISHED 10 August 2023

CITATION
Borisova AY and Bohrson WA (2023), How is carbonate crust digested by magma? *Front. Earth Sci.* 11:1186207. doi: 10.3389/feart.2023.1186207

How is carbonate crust digested by magma?

Anastassia Y. Borisova[1]* and Wendy A. Bohrson[2]

[1]Géosciences Environnement Toulouse, Observatoire Midi-Pyrénées, Université Toulouse III/CNRS/IRD/CNES, Toulouse, France, [2]Department of Geology and Geological Engineering, Colorado School of Mines, Golden, CO, United States

Magma's volatile budget depends on deep magmatic sources, the degree of differentiation and degassing conditions, and volatile input from the assimilated crust. It is, therefore, important to know the exact mechanism by which the crust is assimilated into magma to understand volatile budgets and eruption behavior. To explore reactions between carbonate, calc–silicate, or skarn xenoliths and basaltic andesite magma, we studied ten calc–silicate xenoliths from the 1994, 1998, 2006, and 2010 Merapi eruptions and four sediment samples of local Javanese carbonate crust. An *in situ* electron probe microanalysis of the 1994–2010 calc–silicate xenolith minerals and glasses suggests that calcite is a minor and metastable mineral phase in association with wollastonite. In addition, carbonate melts quenched to calcic glasses (32 ± 7 wt% SiO_2; 38 ± 3 wt% CaO), similar to experimental glasses produced by crust–melt interaction experiments. Thermodynamic modeling using rhyolite MELTS (version 1.2.0) predicts the production of highly silicic (up to ~84 wt% of SiO_2) and CaO-rich (up to ~25 wt %) melts during partial melting of calc–silicate material. The observed mechanism of calc–silicate xenolith assimilation is the generation of highly silicic (77 ± 4 wt% of SiO_2) melts in association with idiomorphic diopside [$Wo_{49}En_{29}$; 57 ± 3 Mg# = $Mg/(Mg+Fe^{2+})$] and other calcic pyroxenes (Wo_{54-82} En_{2-21}; 16–43 Mg#) due to partial melting of xenolith and incongruent dissolution reactions. We hypothesize that the rate-limiting process is the subsequent mixing of the produced crustal melts with representative resident andesitic melt (average 65 wt% SiO_2) through chemical diffusion, which explains major and volatile (Cl) element contents in the Merapi glass products. In addition to high Sr contents and radiogenic $^{87}Sr/^{86}Sr$ and elevated CO_2, Ba, Co, Cr, Cu, V, Zn, and Zr contents in the magmatic minerals and associated glasses, the recrystallized and residual metamorphic sphene, quartz, garnet, and apatite predicted by rhyolite-MELTS or Magma Chamber Simulator modeling during wallrock melting and residual metastable calcite and wollastonite are important tracers of calc–silicate crust assimilation. The disequilibrium process of calc–silicate crustal assimilation can, thus, be well predicted by dissolution experiments and thermodynamic modeling using rhyolite-MELTS or Magma Chamber Simulator. The rate of calc–silicate crustal assimilation is still unconstrained without adequate high-temperature kinetic time-series experiments. We predict that the crustal assimilation rate is controlled by the Si–Al diffusion and associated convection in the hydrous silicate magma.

KEYWORDS

crustal assimilation, kinetics, mechanism, rate, carbonate crust, calc-silicate xenolith, mineral dissolution, silicic melts

Introduction

Decarbonation of the arc-crust beneath Merapi may magnify the volcanic CO_2 output and potentially contribute to the volcano's eruption behavior (Borisova et al., 2013, 2016; Erdmann et al., 2014, 2016; Deegan et al., 2023). Numerous experimental works devoted to pure carbonate solubility in mafic melts demonstrated the important role that the addition of carbonate material has on the magma liquidus phase stability field (Freda et al., 2008; Iacono-Marziano et al., 2008, 2009; Mollo et al., 2010). Deegan et al. (2010), Jolis et al. (2013), and Blythe et al. (2015) experimentally studied the interaction of carbonate materials with mafic and alkaline melts at conditions corresponding to the deep crust. They discovered that the direct interaction of carbonates with the silicate melt is rapid (minutes), with the outcome being the formation of Ca-rich carbonate melts. Chadwick et al. (2007) documented the formation of Ca-rich glasses in calc–silicate xenoliths that were assimilated by the 1994–1998 Merapi (Indonesia) magmas. Costa et al. (2013), Borisova et al. (2013; 2016) and Troll et al. (2013) studied the lava, ash, xenolith, and igneous samples of recent Merapi eruptions. Geochemical and detailed *in situ* data on the glasses and minerals confirm an important effect that the crustal level (~200 MPa depths, Borisova et al., 2013; Erdmann et al., 2016) assimilation of crustal calc–silicate xenoliths has on the 2010 basaltic andesite magma. The pre-eruptive saturation of the basaltic andesite magma with aqueous carbonic NaCl–HCl-bearing fluid was suggested to be responsible for the high explosivity of the Merapi volcano in 2010. Both Nadeau et al. (2011; 2013a, b) and Troll et al. (2013) showed that glass inclusions in Merapi's phenocrysts are typically CO_2-rich. Alternatively, it was proposed that an unusually large batch of recharge magma could also have triggered the 2010 eruption (Costa et al., 2013; Jousset et al., 2013).

A mechanism of crustal assimilation has been suggested by Borisova et al. (2013): 1) contact metamorphism of Javanese sediments and formation of calc–silicate skarns like xenoliths in the 1998 and 2006 eruptions; 2) assimilation of the calc–silicate xenoliths through complete digestion, partial melting, or dissolution (partial melting involves reaction of a mineral to silicate melt, whereas mineral dissolution happens in the presence of silicate melt) and generation of calcic melts like those defined by Borisova et al. (2016) (referred to as the 2010 Crustal Assimilant); and 3) effective mixing between hydrous K-rich (resident) melt and the 2010 Crustal Assimilant (CaO up to 10.5 wt% and CaO/Al_2O_3 up to 1.2) melts that are characterized by crustal signatures, followed by crystallization. However, the kinetics (rates and mechanisms) of the assimilation mechanisms occurring in the Merapi pre-eruptive system have not been constrained yet. Mechanisms of xenolith dissolution and/or partial melting in the resident basaltic andesite magma may be recorded through detailed investigation of crustal calc–silicate xenoliths. Finally, Whitley et al. (2020) performed a detailed investigation of the Merapi calc–silicate xenolith production; however, no modeling of partial melting of potential calc–silicate wallrock has been applied. Our work here investigates mechanisms of the crustal assimilation affecting the Merapi basaltic andesite magmas based on detailed petrologic, mineralogical, and geochemical investigations coupled with rhyolite-MELTS thermodynamic modeling (Gualda et al., 2012; Ghiorso and Gualda, 2015). The results demonstrated in this work have implications for explosive volcanism related to crustal carbonate assimilation (e.g., volcanoes Merapi and Kelut, Indonesia).

Geological background

Merapi stratovolcano is located ~30 km north of the city of Yogyakarta, Indonesia. The volcano is composed mainly of basaltic-andesite tephra, pyroclastic flows, lava, and lahar deposits. Since the 19th century, Merapi has erupted every 4–6 years, with most of these eruptions having explosivity indices ≤VEI 2 (Volcanic Explosivity Index), although moderate VEI 1–3 (1832, 1849, 1930, 1961, 2014, and 2018) and large VEI 4 (2010) eruptions have also occurred (https://volcano.si.edu/). The recent activity of Merapi is characterized by 1) recurrent effusive growth of viscous lava domes that collapse to form pyroclastic currents, referred to as the Merapi-type block-and-ash flows (BAFs) (VEI 2) and 2) more exceptional explosive eruptions of the sub-Plinian type (VEI 3–4) associated with columns collapsing into pumice-and-ash pyroclastic flows (Voight et al., 2000). The explosive eruption of 2010 (Costa et al., 2013) marks an important change in Merapi's activity toward more explosive behavior. Today, Merapi has reverted to more typical behavior since, i.e., relatively abundant eruptions at VEI 1–3.

Merapi is located on the carbonate crust of 8–10 km thickness of the Kendeng basin, where Cretaceous to Cenozoic volcanoclastic sediments are overlain by shallow marine limestones, all of which overlie arc and ophiolite basement rocks (Smyth et al., 2005). Recent detailed micro-analytical and experimental data suggest the effects of shallow-level assimilation of the local Javanese sedimentary crust are significant (Chadwick et al., 2007; Deegan et al., 2010; Deegan et al., 2010; Borisova et al., 2013, 2016; Troll et al., 2013). Carbonate crust assimilation can play a key role in producing highly explosive fluid-saturated magmas (Iacono-Marziano et al., 2008, 2009; Deegan et al., 2010; Borisova et al., 2013; Troll et al., 2013). To evaluate the mechanisms and rates of crustal assimilation, we analyzed major, trace, and volatile elements and Sr–Nd–Pb isotopes in the Javanese crust and Merapi xenoliths and their minerals and glasses, using state-of-the-art analytical methods. Based on these data, we propose a mechanism of crustal assimilation preceding and triggering the Merapi eruptions.

Materials and methods

1994–2010 Merapi sample collection

The 1994, 1998, 2006, and 2010 xenolith sample list is shown in Table 1. M94-CS-104 and M94-CS-106 are from the 1994 small-volume Merapi-type BAFs. Samples MXCS-1, MXCS-2, MXCS-4, MXCS-7, and MXCS-9 are from the 1998 BAFs. MXCS-06-KAT2 is a calc–silicate xenolith from the 2006 eruption, and 014-1B is from the 2010 eruption. Samples of the 2010 Merapi xenoliths were collected during the 2015 French expedition (Borisova et al., 2016). LST-1, LST-2, LST-3, and LST-4 are carbonate sediment samples from Parangtritis beach (Java, Indonesia). The sampling locations are shown in the study of Deegan et al. (2010). More details on the samples can be found in the study of Chadwick (2008), Table 2, and Table 3.

TABLE 1 Merapi calc–silicate xenolith location, sampling, and mineralogy details.

Sample:	M94-CS-104	M94-CS-106	MXCS-1	MXCS-2	MXCS-4	MXCS-7	MXCS-9	MXCS-06-KAT2	014-1B (SEMO-3)	LST-1	LST-2	LST-3	LST-4
Rock type:					calc-silicate xenoliths						carbonate sediments		
Figure:	2A			2(B, D)				2(C)	2(E-H)				
Eruption year:	1994	1994	1998	1998	1998	1998	1998	2006	2010	-	-	-	-
Sampling:	(1)	(1)	(1)	(1)	(1)	(1)	(1)	(1)	this work	(2,3)	(2,3)	(2,3)	(2,3)
Mineralogy:													
Cc	+	N.A.	-	N.A.	-	N.A.	N.A.	-	-	+	+	+	+
Larn	+	N.A.	-	N.A.	-	N.A.	N.A.	-	-	N.A.	N.A.	N.A.	-
Srbr	+	N.A.	-	N.A.	-	N.A.	N.A.	-	-	N.A.	N.A.	N.A.	-
Wo	+	N.A.	+	N.A.	-	N.A.	N.A.	+	+	N.A.	N.A.	N.A.	-
Di	-	N.A.	+	N.A.	±	N.A.	N.A.	+	+	N.A.	N.A.	N.A.	-
Heden	-	N.A.	+	N.A.	±	N.A.	N.A.	+	+	N.A.	N.A.	N.A.	-
An	-	N.A.	+	N.A.	+	N.A.	N.A.	-	+	N.A.	N.A.	N.A.	+
Qtz	-	N.A.	-	N.A.	+	N.A.	N.A.	-	-	N.A.	N.A.	N.A.	±
Gross	-	N.A.	-	N.A.	-	N.A.	N.A.	-	-	N.A.	N.A.	N.A.	-
FeTi oxides	±	N.A.	±	N.A.	±	N.A.	N.A.	+	+	N.A.	N.A.	N.A.	-
Sph	-	N.A.	+	N.A.	-	N.A.	N.A.	+	±	N.A.	N.A.	N.A.	-
Sulf	-	N.A.	+	N.A.	-	N.A.	N.A.	-	-	N.A.	N.A.	N.A.	-
Apt	-	N.A.	+	N.A.	-	N.A.	N.A.	+	-	N.A.	N.A.	N.A.	-
Glass	-	N.A.	+	N.A.	-	N.A.	N.A.	+	+	N.A.	N.A.	N.A.	-
Clay	-	N.A.	-	N.A.	-	N.A.	N.A.	+	-	N.A.	N.A.	N.A.	+

References for geographic location: (1) Troll et al. (2013); (2) Deegan et al. (2010); (3) Chadwick (2008). Cc, calcite; Larn, larnite; Srbr, srebrodolskite; Wo, wollastonite; Di, diopside; Hedenb, hedenberite; An, anorthite; Qtz, quartz; Gross, grossular; Sph, sphene; Sulf, sulfides; Apt, apatite; Glass, glasses; Clay, clay minerals. +: present and -: absent in the sample; N.A., not analyzed; (+), irregular presence.

10.3389/feart.2023.1186207

TABLE 2 Volatile, major, and trace element and isotopic composition of the bulk Merapi calc–silicate xenolith and Javanese limestone samples.

Sample	MXCS-1R	MXCS-1C	M-XCS-1	MXCS-2	MXCS-4	MXCS-7R	MXCS-7C	MXCS-9	M-94-CS-104	M94-CS-106	MXCS-06-KAT2	LST-1	LST-2	LST-3	LST-4
SiO_2, wt%	48.11	58.38	52.73	69.44	82.49	53.30	52.61	48.55	48.32	48.27	54.05	0.24	0.19	0.37	46.42
TiO_2	0.50	0.03	0.072	0.49	0.48	0.63	0.17	0.62	0.23	0.31	0.13	D.L.	D.L.	D.L.	0.54
Al_2O_3	10.52	0.63	1.53	12.45	4.55	14.11	5.09	15.77	5.33	9.88	1.56	0.13	0.13	0.18	11.47
Fe_2O_3	11.31	1.67	3.81	4.14	2.75	8.23	3.63	7.80	2.06	3.23	1.73	0.04	0.03	0.06	5.50
MgO	5.84	0.57	1.13	1.76	0.72	3.10	0.86	3.55	0.88	0.89	0.40	0.29	0.28	0.31	2.15
MnO	0.32	0.19	0.24	0.11	0.11	0.25	0.26	0.22	0.078	0.14	0.23	0.00	0.01	0.00	0.19
CaO	21.56	36.75	39.73	8.37	8.52	17.11	34.64	21.70	39.82	35.11	40.21	55.39	55.17	55.00	11.89
Na_2O	0.54	0.02	0.05	1.84	0.16	2.14	0.77	1.15	0.43	0.48	0.32	0.02	0.01	0.02	1.03
K_2O	0.33	0.01	0.02	0.22	0.02	0.83	0.65	0.33	0.16	0.56	0.35	0.01	0.01	0.01	1.06
P_2O_5	0.17	0.03	D.L.	0.11	0.05	0.19	0.04	0.18	0.09	0.10	D.L.	D.L.	D.L.	D.L.	0.13
LOI	0.10	1.17	0.23	−0.13	−0.16	−0.30	0.47	−0.10	1.69	0.49	0.17	43.69	43.71	43.72	19.44
Total	99.29	99.43	99.54	98.79	99.67	99.58	99.18	99.76	99.10	99.46	99.14	99.80	99.52	99.68	99.81
CO_2 total	0.30	0.83	0.29	0.15	0.17	0.25	0.50	0.20	1.16	0.18	0.03	43.68	44.00	43.86	7.79
H_2O total	0.36	0.24	0.26	0.11	0.07	0.13	0.24	0.21	0.60	0.22	0.16	0.32	0.32	0.43	11.78
S total	0.55	<0.01	0.03	0.03	0.01	0.06	0.02	<0.01	0.02	<0.01	<0.01	<0.01	0.02	0.02	0.01
Cl, ppm	175	<20	N.A.	<20	<20	42	29	185	N.A.	N.A.	N.A.	140	22	125	N.A.
As	D.L.	D.L.	D.L.	1.972	5.541	2.915	1.329	1.315	D.L.	3.79	D.L.	D.L.	D.L.	D.L.	3.11
Ba	100.4	1.882	8.1	212.6	171.3	240	110.5	122.9	65.1	326	37.4	2.172	4.374	3.218	106
Be	0.78	D.L.	D.L.	0.779	D.L.	1.056	0.472	1.382	D.L.	1.03	D.L.	D.L.	D.L.	D.L.	0.68
Bi	D.L.	D.L.	D.L.	D.L.	D.L.	D.L.	D.L.	D.L.	D.L.	D.L.	D.L.	D.L.	D.L.	D.L.	0.13
Cd	0.253	0.352	0.43	0.148	0.252	0.182	0.395	0.356	0.39	0.31	0.30	D.L.	D.L.	0.121	0.14
Ce	20.98	5.07	5.94	24.27	30.5	25.52	13.58	26.64	11.2	32.4	9.99	0.541	0.625	0.667	19.8
Co	118.7	59.54	7.03	80.04	86.32	67.89	56.46	72.42	4.76	4.93	3.25	0.617	0.76	0.644	5.73
Cr	49.76	D.L.	7.7	89.05	674.2	79.27	6.809	19.92	22.9	5.6	26.1	5.234	8.375	D.L.	12.3
Cs	0.792	D.L.	0.26	0.52	0.179	2.095	2.45	0.512	0.33	3.68	0.73	D.L.	D.L.	D.L.	1.59
Cu	158.1	D.L.	7.9	19.3	D.L.	244.9	42.03	5.354	19.1	10.5	6.8	D.L.	D.L.	D.L.	45.4
Dy	2.844	2.837	3.78	2.97	3.927	2.713	1.618	3.971	1.46	2.80	1.26	0.157	0.19	0.2	5.22

(Continued on following page)

10.3389/feart.2023.1186207

TABLE 2 (*Continued*) Volatile, major, and trace element and isotopic composition of the bulk Merapi calc–silicate xenolith and Javanese limestone samples.

Sample	MXCS-1R	MXCS-1C	M-XCS-1	MXCS-2	MXCS-4	MXCS-7R	MXCS-7C	MXCS-9	M-94-CS-104	M94-CS-106	MXCS-06-KAT2	LST-1	LST-2	LST-3	LST-4
Er	1.533	1.26	1.79	1.728	2.092	1.666	1.029	2.464	0.886	1.77	0.788	0.09	0.117	0.104	3.34
Eu	1.819	1.73	1.53	0.906	0.948	0.848	0.598	1.063	0.317	0.967	0.696	0.047	0.048	0.053	1.08
Ga	12.03	0.729	1.80	11.31	4.553	16.08	5.427	18.31	6.04	10.9	2.10	D.L.	D.L.	D.L.	12.9
Gd	3.464	3.189	3.64	3.09	3.707	2.886	1.597	3.925	1.43	2.85	1.26	0.181	0.201	0.22	4.37
Ge	1.707	1.152	1.15	1.151	1.401	1.349	0.884	1.411	1.08	0.81	0.50	D.L.	D.L.	D.L.	1.21
Hf	2.194	D.L.	0.34	2.553	6.538	2.345	1.005	3.132	1.23	3.15	0.53	D.L.	D.L.	D.L.	3.02
Ho	0.545	0.503	0.748	0.608	0.761	0.554	0.341	0.846	0.325	0.634	0.291	0.032	0.042	0.038	1.21
In	0.117	D.L.	D.L.	D.L.	D.L.	0.121	D.L.	D.L.	D.L.	D.L.	D.L.	D.L.	D.L.	D.L.	0.09
La	10.18	1.807	2.21	11.36	14.29	11.9	6.297	14.34	5.58	16.4	4.82	0.629	0.771	0.75	8.48
Lu	0.248	0.111	0.161	0.27	0.29	0.288	0.176	0.419	0.128	0.320	0.125	0.01	0.014	0.014	0.555
Mo	0.734	D.L.	D.L.	D.L.	D.L.	1.216	0.695	D.L.	D.L.	0.87	D.L.	D.L.	D.L.	D.L.	0.70
Nb	3.796	0.328	0.54	3.839	5.841	5.132	1.973	2.709	3.08	3.38	1.06	D.L.	D.L.	D.L.	1.41
Nd	12.43	5.697	5.61	13.39	15.92	13.32	7.182	15.96	6.10	14.8	5.48	0.639	0.73	0.766	14.4
Ni	32.5	6.887	13.7	23.71	47.1	41.13	11.63	21.08	8.7	6.0	13.2	D.L.	D.L.	D.L.	11.0
Pb	3.006	0.7216	1.44	7.67	3.9157	6.5409	2.917	3.585	2.13	8.76	3.01	D.L.	D.L.	D.L.	5.98
Pr	2.579	0.854	0.969	2.94	3.656	2.977	1.591	3.456	1.46	3.78	1.31	0.129	0.153	0.156	3.05
Rb	10.66	D.L.	1.12	3.129	0.466	18.97	17.5	6.836	3.79	32.1	10.2	D.L.	D.L.	D.L.	26.6
Sc	13.25	3.45	4.46	11.56	7.01	18.38	3.33	15.54	5.31	3.71	2.77	D.L.	D.L.	D.L.	17.7
Sb	D.L.	D.L.	D.L.	D.L.	0.332	D.L.	D.L.	D.L.	D.L.	0.27	D.L.	D.L.	D.L.	D.L.	0.26
Sm	3.518	2.751	3.09	2.966	3.65	2.933	1.601	3.801	1.45	3.24	1.25	0.144	0.17	0.187	4.04
Sn	0.875	D.L.	0.50	0.749	1.312	0.827	0.5	1.458	D.L.	1.08	0.57	D.L.	D.L.	D.L.	1.18
Sr	681.8	410.2	442	323	154	396.8	222.4	418.9	206	289	190	122.8	176.5	122.4	338
Ta	1.517	0.756	0.05	1.257	1.55	1.06	0.755	0.98	0.19	0.30	0.09	D.L.	D.L.	D.L.	0.14
Tb	0.499	0.492	0.613	0.481	0.634	0.454	0.258	0.635	0.229	0.447	0.187	0.026	0.03	0.032	0.764
Th	3.373	0.263	0.99	3.434	3.953	4.459	2.572	6.882	2.46	7.36	1.08	0.032	0.036	0.04	1.73
Tm	0.228	0.157	0.222	0.256	0.304	0.258	0.166	0.388	0.127	0.277	0.116	0.012	0.017	0.015	0.508
U	1.259	0.116	0.58	0.888	1.083	1.173	0.665	1.822	5.40	2.58	0.43	0.809	0.426	0.519	2.75

(Continued on following page)

10.3389/feart.2023.1186207

TABLE 2 (*Continued*) Volatile, major, and trace element and isotopic composition of the bulk Merapi calc–silicate xenolith and Javanese limestone samples.

Sample	MXCS-1R	MXCS-1C	M-XCS-1	MXCS-2	MXCS-4	MXCS-7R	MXCS-7C	MXCS-9	M-94-CS-104	M94-CS-106	MXCS-06-KAT2	LST-1	LST-2	LST-3	LST-4
V	82.58	4.47	14.0	66	33.1	138.7	25.2	114.9	53.4	32	14.1	2.4	1.956	2.243	62.5
W	N.A.	N.A.	0.58	N.A.	N.A.	N.A.	N.A.	N.A.	0.45	0.70	0.46	D.L.	D.L.	D.L.	0.45
Y	16.97	18.1	23.9	19.05	26.12	16.6	11.1	25.81	10.8	18.0	9.48	1.479	1.957	1.715	32.9
Yb	1.551	0.905	1.30	1.732	1.941	1.774	1.146	2.669	0.820	1.96	0.805	0.071	0.097	0.088	3.53
Zn	113	20.29	42.6	48.13	46.4	104.7	42.91	100.6	20.3	51.0	21.6	D.L.	D.L.	D.L.	71.1
Zr	87.81	3.262	11.4	101.4	298.2	83.84	42.78	122.8	41.3	121	18.5	D.L.	1.111	D.L.	95.8

Sample	MXCS-1R	MXCS-1C	MXCS-2	MXCS-4	MXCS-7R	MXCS-7C	MXCS-9	LST-1	LST-2	LST-3
$^{87}Sr/^{86}Sr$	0.709376	0.707985	0.705843	0.707387	0.705946	0.705945	0.706840	0.708788	0.708751	0.708789
error (2σ)	0.000016	0.000024	0.000016	0.000010	0.000014	0.000010	0.000006	0.000018	0.000006	0.000020
$^{143}Nd/^{144}Nd$	0.512555	0.512625	0.512779	0.512503	0.512748	0.512755	0.512778	0.512488	0.512536	0.512379
error (2σ)	0.000018	0.000024	0.000015	0.000009	0.000014	0.000013	0.000010	0.000037	0.000029	0.000049
$^{206}Pb/^{204}Pb$	18.5576	18.4910	18.6056	18.6388	18.6635	18.6338	18.5802	N.A.	N.A.	N.A.
error (2σ)	0.0033	0.0056	0.0007	0.0010	0.0009	0.0016	0.0009	N.A.	N.A.	N.A.
$^{207}Pb/^{204}Pb$	15.5310	15.5747	15.5886	15.5243	15.6180	15.6029	15.6012	N.A.	N.A.	N.A.
error (2σ)	0.0031	0.0056	0.0007	0.0009	0.0008	0.0017	0.0010	N.A.	N.A.	N.A.
$^{208}Pb/^{204}Pb$	38.676	38.863	38.757	38.790	38.937	38.891	38.972	N.A.	N.A.	N.A.
error (2σ)	0.008	0.015	0.002	0.003	0.002	0.005	0.003	N.A.	N.A.	N.A.
$^{207}Pb/^{206}Pb$	0.83695	0.84230	0.83783	0.83290	0.83683	0.83744	0.83749	N.A.	N.A.	N.A.
error (2σ)	0.00024	0.00026	0.00006	0.00004	0.00004	0.00011	0.00008	N.A.	N.A.	N.A.
$^{206}Pb/^{207}Pb$	1.19482	1.18722	1.19355	1.20063	1.19498	1.19412	1.19404	N.A.	N.A.	N.A.
error (2σ)	0.00024	0.00026	0.00006	0.00004	0.00004	0.00011	0.00008	N.A.	N.A.	N.A.
$^{208}Pb/^{206}Pb$	2.08417	2.10184	2.08300	2.08110	2.08628	2.08740	2.08773	N.A.	N.A.	N.A.
error (2σ)	0,00006	0,00006	0,00001	0,00001	0,00001	0,00002	0,00002	N.A.	N.A.	N.A.

D.L., contents below the detection limit; N.A., values not analyzed.

10.3389/feart.2023.1186207

Volatile, major, and trace elements and Sr–Nd–Pb isotopic composition of the bulk xenolith and sediment samples

Volatile concentrations of CO_2 and S were measured at SARM (Service d'Analyse des Roches et des Minéraux, Centre de Recherches Pétrographiques et Géochimiques, Vandoeuvre-ès-Nancy, France) using a Leco SC-144DR sulfur and carbon analyzer, by heating at 1400°C with oxygen flux and infrared (IR) detection. H_2O concentrations were measured using Karl Fischer titration. Major and trace elements were measured by inductively coupled plasma optical emission spectroscopy (ICP–OES) and ICP–MS, using a method developed at SARM (Carignan et al., 2001) employing an ICP–OES IRIS Advantage ERS from Thermo Scientific and an ICP–MS x7 from Thermo Scientific without pre-concentration of rare earth elements (REEs) and U/Th.

For Sr–Nd–Pb isotope measurements at SARM, 100–200 mg of very fine rock powder (particle size <50 mm) was placed into a 15 mL Savillex beaker. A mixture of concentrated sub-boiled HNO_3 (4 mL) and ultrapure HF (1 mL) was added to the powder samples. The solutions were kept at 115°C for 24–48 h, then evaporated, re-filled with concentrated HCl, and heated for 24 h to ensure complete digestion of the powder samples. The samples were then split into two parts and dried prior to purification of the elements.

For chromatographic separation of Pb from the matrix, 1 mL of HBr (0.8 M) was added to the aliquots. The chromatographic micro-column was filled with AG1X8 resin. The matrix was eluted with 0.8 M HBr, and Pb was recovered with 6 M HCl, following a method similar to that in the study of Manhès et al. (1980). Isotopic analysis was conducted using multicollector–inductively coupled plasma–mass spectrometry (MC–ICP–MS) (Micromass IsoProbe) using a Tl (NIST 997) spike to correct instrumental mass bias. Tl and Pb isotope values used for the NIST 981 and NIST 977 reference materials were those obtained by Thirlwall (2002). More details on the method are described by Cloquet et al. (2006).

For Sr and Nd isolation, the samples were diluted with 2 mL of 2 M HNO_3, following the analytical protocol of Pin et al. (1994). An additional stage of further isolation of Nd from Sm was applied using Ln spec resin, following the procedure described by Pin et al. (1994). Strontium isotopes were measured using a thermal ionization mass spectrometer (TIMS; Triton Plus, from Thermo Electron) in the multicollection mode. In addition, five Faraday cups were used to monitor Rb. Sr was loaded onto a Re filament. Internal normalization using $^{86}Sr/^{88}Sr$ (0.1194) and the exponential law were used to correct the instrumental mass bias. NBS 987 was used to control methodological accuracy. The average blanks were negligible compared to the Sr concentration in the samples (average of 300 pg for Sr). Nd isotopes were measured using MC–ICP–MS (Micromass IsoProbe). To control instrumental mass bias, we applied a constant $^{146}Nd/^{144}Nd$ (0.72190) (Luais et al., 1997) and the exponential law. Reference JMC Nd was used to control methodological accuracy. The average blank corresponded to about 100 pg of Nd, which is negligible compared to the Nd concentration of the sample. Results of bulk rock Sr–Nd–Pb isotope analyses are summarized in Table 2 and Figure 1.

Volatile, major, and minor element composition of the xenolith minerals and glasses

Major element analyses of minerals and glasses and backscattered electron images of the samples were performed at the Géosciences Environnement Toulouse (GET, Toulouse, France) laboratory and at the Centre de MicroCaractérisation Raimond Castaing (Toulouse, France). The main phases in the samples were identified using a scanning electron microscope (SEM) JEOL JSM-6360 LV coupled with energy-dispersive X-ray spectroscopy (EDS) (Borisova et al., 2013; Figure 2). The major, minor, and Cl contents of the crystals and glasses were analyzed using a CAMECA SX-Five microprobe. In general, beam conditions were 15 kV accelerating voltage and 10 or 20 nA probe current. For the analysis of glasses, the CAMECA SX-Five was used following the method of Borisova et al. (2010). The beam (15 kV and 10 nA) was set to a 10 μm beam diameter where possible. Sodium was analyzed first to ensure minimal loss during EPMA. These analytical conditions allowed an optimal signal for the major and minor elements, good internal precision, and minimal sodium loss during EPMA. The following synthetic and natural standards were used for calibration: albite (Na), corundum (Al), wollastonite (Si, Ca), sanidine (K), pyrophanite (Mn, Ti), hematite (Fe), periclase (Mg), and tugtupite (Cl). Element and background counting times for most analyzed elements were 10 s (except for 5 s for Na and K) and 5 s, respectively, whereas peak counting time was 120 s for Cl. The detection limit for Cl was 70 ppm. The silicate reference materials of MPI-DING covering ultramafic to felsic compositions (GOR132-G, GOR128-G, KL2-G, ML3B-G, and ATHO-G of the study of Jochum et al. (2006)) were analyzed as unknown samples to monitor analytical accuracy (Borisova et al., 2012, 2010). The estimated accuracy ranges from 0.5% to 3% (1σ RSD = relative standard deviation), depending on the element contents in the reference glasses. Additionally, the analysis of reference silicate material allowed us to estimate the analytical precision for the major and minor elements (e.g., Cl in glasses). The precision estimated in this way is compatible with the microprobe analytical uncertainty (derived from counting statistics).

Thermodynamic modeling by rhyolite-MELTS or Magma Chamber Simulator

Thermodynamic modeling using rhyolite-MELTS (Gualda et al., 2012; Ghiorso and Gualda, 2015) was performed to estimate the compositions of partial melts of representative calc–silicate crust. Rhyolite-MELTS is based on calibrations informed by experiments and constraints from natural silicic magma systems. For detailed model information, see the aforementioned references. Like all thermodynamic models, rhyolite-MELTS results must be carefully assessed to evaluate their applicability to natural systems. This includes comparing the resulting partial melts with compositions of observed products, such as the Si-rich glasses documented in this work.

In the thermodynamic modeling of the wallrock partial melting using rhyolite-MELTS (Gualda et al., 2012; Ghiorso and Gualda, 2015) or Magma Chamber Simulator MCS (Bohrson et al., 2014,

TABLE 3 Average composition of minerals and glasses in the Merapi calc–silicate xenoliths.

Sample:	M94-CS-104	M94-CS-104	M94-CS-104	M94-CS-104	M94-CS-104	MXCS1 and 014-1B	MXCS1	MXCS1 and 014-1B	MXCS1
Phase:	Calcite (3)	Srebrodolskite (2)	Larnite (3)	Wollastonite (8)	Calcic glass (3)	Wollastonite (3)	Hedenbergite (7)	Silicic glass (18)	Diopside (3)
Caption:	Cc	Srbr	Larn	Wo	Ca glass	Wo	Heden	Si glass	Di
Formula:	$CaCO_3$	$Ca_2Fe^{3+}{}_2O_5$	Ca_2SiO_4	$CaSiO_3$	-	$CaSiO_3$	$CaFe_2+Si_2O_6$	-	$CaMgSi_2O_6$
SiO_2	D.L.	0.32 ± 0.08	35.1 ± 0.3	52.0 ± 0.4	31.73 ± 6.80	52.1 ± 0.3	50.6 ± 0.6	76.5 ± 3.5	53.3 ± 0.5
TiO_2	D.L.	D.L.	D.L.	D.L.	D.L.	0.13 ± 0.03	0.06 ± 0.08	0.22 ± 0.10	0.04 ± 0.06
Al_2O_3	D.L.	D.L.	D.L.	D.L.	0.07 ± 0.08	D.L.	0.28 ± 0.07	12.3 ± 3.2	0.4 ± 0.1
FeO_{bulk}	0.07 ± 0.06	50.3 ± 0.3	D.L.	0.2 ± 0.4	0.13 ± 0.08	1.8 ± 0.5	20.5 ± 2.3	1.8 ± 0.8	14.0 ± 1.1
$Fe_2O_{3\ calc}$[a]	-	55.9 ± 0.3	-	0.5 ± 0.7	-	0.01 ± 0.02	0.69 ± 0.67	-	-
MnO	0.08 ± 0.07	0.7 ± 0.4	D.L.	0.07 ± 0.06	0.01 ± 0.02	0.22 ± 0.06	0.43 ± 0.08	0.07 ± 0.06	0.5 ± 0.1
MgO	D.L.	D.L.	D.L.	0.10 ± 0.08	1.15 ± 1.90	0.13 ± 0.01	5.2 ± 1.5	D.L.	10.3 ± 0.6
CaO	59.8 ± 1.3	D.L.	65.1 ± 1.1	48.5 ± 0.5	37.76 ± 3.14	46.9 ± 0.2	23.5 ± 0.4	4.3 ± 2.2	24.1 ± 0.3
Na_2O	D.L.	D.L.	D.L.	D.L.	0.14 ± 0.06	D.L.	0.03 ± 0.03	2.6 ± 0.4	0.02 ± 0.04
K_2O	D.L.	D.L.	D.L.	D.L.	0.03 ± 0.02	D.L.	0.01 ± 0.01	3.1 ± 0.7	0.02 ± 0.01
P_2O_5	D.L.	D.L.	D.L.	D.L.	0.06 ± 0.04	D.L.	D.L.	0.03 ± 0.03	D.L.
Cl	D.L.	D.L.	D.L.	D.L.	D.L.	D.L.	D.L.	0.07 ± 0.04	D.L.
Total	61.1 ± 2.2	92.96 ± 0.01	100.4 ± 0.7	101.6 ± 0.8	71.12 ± 1.81	101.3 ± 0.6	101.4 ± 0.6	101.0 ± 1.1	101.5 ± 0.9
H_2O+CO_2	38.9 ± 2.2.	7.04 ± 0.01	-	-	28.9 ± 1.8	-	-	-	-
Wo [b]	-	-	-	99.4 ± 0.7	-	96.7 ± 0.8	50.3 ± 0.5	-	48.9 ± 0.3
En	-	-	-	0.3 ± 0.2	-	0.37 ± 0.03	15.5 ± 4.2	-	29.0 ± 1.7
Fs	-	-	-	0.4 ± 0.6	-	2.9 ± 0.8	34.2 ± 4.2	-	22.1 ± 1.8
$Mg^{\#}$	-	-	-	22.3 ± 14.4	-	11.5 ± 2.3	30.5 ± 7.9	-	56.7 ± 3.4

The numbers represent the average content (bracketed number is the amount of analytical points per phase) with 2σ standard deviation, reflecting the chemical heterogeneity.

[a]Fe2O3 content is calculated. Fe2O3 content in srebrodolskite is the value calculated from the measured FeO content. Both FeO and Fe2O3 contents are calculated values in pyroxenes based on the chemical formula XY(Si,Al)2O6 (where X represents the ions of Ca, Na, Fe^{2+}, Mg, and Mn and Y represents the ions of Al, Fe^{3+}, and Ti).

[b]Wo is wollastonite, En is enstatite, and Fs is ferrosilite end-members. Mg# is calculated as Mg/(Mg + Fe^{2+}) 100, where Mg and Fe^{2+} are ions per formula unit.

D.L. are values below detection limits.

10.3389/feart.2023.1186207

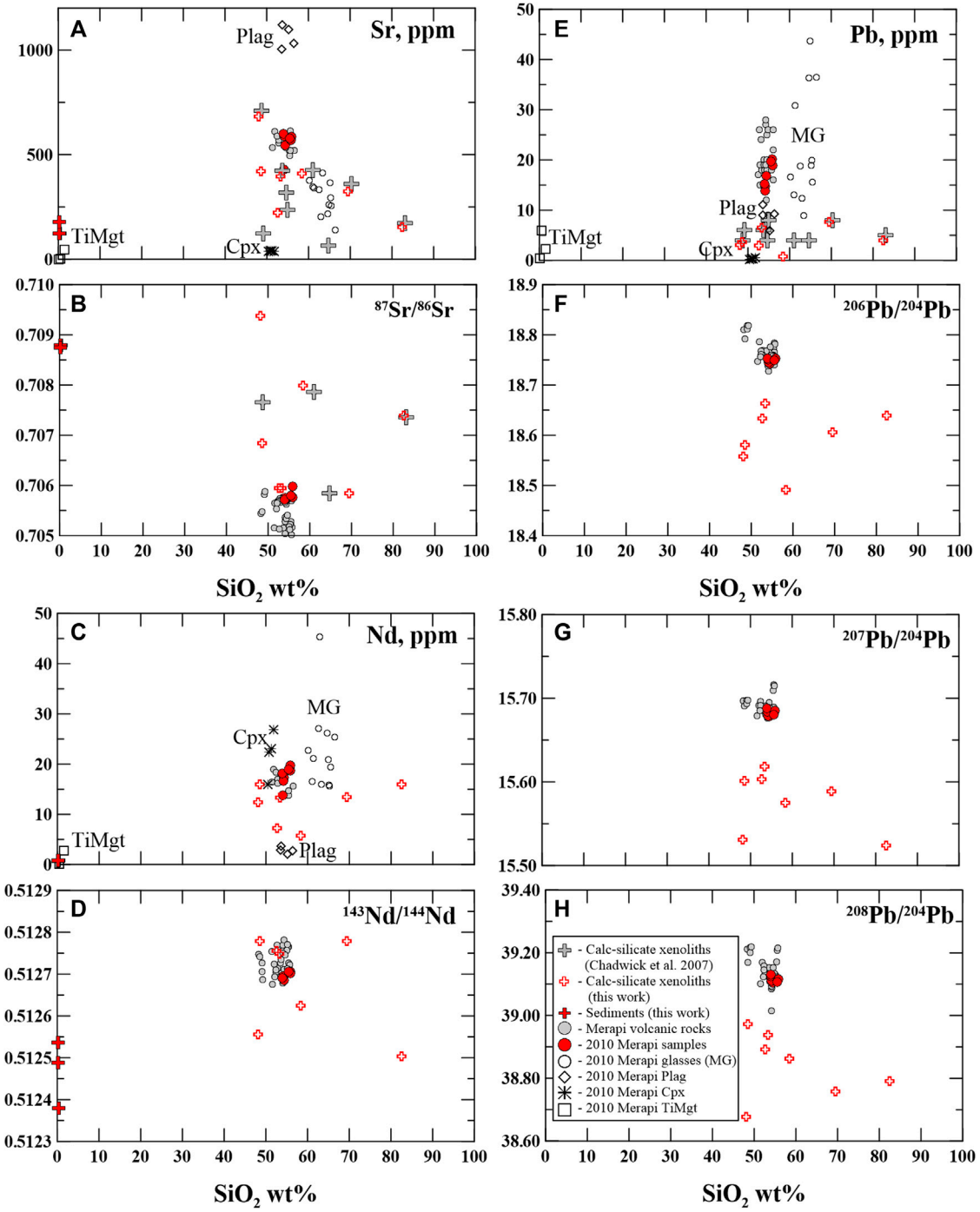

FIGURE 1
(A) Sr (ppm)–SiO_2 (wt%), **(B)** $^{87}Sr/^{86}Sr$–SiO_2 (wt%), **(C)** Nd (ppm)–SiO_2 (wt%), **(D)** $^{143}Nd/^{144}Nd$–SiO_2 (wt%), **(E)** Pb (ppm)–SiO_2 (wt%), **(F)** $^{206}Pb/^{204}Pb$–SiO_2 (wt%), **(G)** $^{207}Pb/^{204}Pb$–SiO_2 (wt%), **(H)** $^{208}Pb/^{204}Pb$–SiO_2 (wt%) in the calc–silicate xenoliths and local Javanese carbonate sediments, the Merapi volcanic rocks, and the 2010 Merapi rocks and matrix glasses. The 2010 Merapi data are according to the study of Borisova et al. (2013), and the previous data on the calc–silicate xenoliths are from the study of Chadwick et al. (2007). Plag - plagioclase, Cpx- clinopyroxene, TiMgt - titanomagnetite. The Merapi volcanic rocks are from the MERAPIDATA database (Borisova et al., 2011).

2020; Heinonen et al., 2020), we used two contrasting compositions (SiO_2-rich and CaO-rich of the 1994–2010 calc–silicate xenoliths Figure 3) from the 1998–2006 Merapi collection (MXCS-1R; MXCS-4, Table 4) as potential crustal contaminants. The bulk compositions (Supplementary Dataset S1) of these two calc–silicate xenoliths underwent equilibrium crystallization (which is the equivalent of equilibrium melting) from the liquidus to the solidus or near solidus. Crystallization/melting occurred in five-degree increments. The resulting partial melts are shown in Figure 4, with the arrow showing the direction of increasing temperature (i.e., wallrock

heating). Additional initial conditions include 200 MPa and Fe_2O_3/FeO ratio = 0.24, according to the results of studies of Costa et al. (2013) and Borisova et al. (2013; 2016).

Results

Compositions of the calc–silicate xenoliths and Javanese sediment samples

Javanese carbonate sediments are strongly enriched in volatiles, mostly in CO_2 (8–44 wt%) and H_2O (0.3–11.8 wt%) contents, compared to calc–silicate xenoliths (0.03–1.2 wt% CO_{2total} and 0.1–0.6 wt% H_2O_{total} contents). Both types of rock samples demonstrate similar low chlorine contents, 22–140 ppm for sediments and up to 185 ppm for xenoliths, whereas sulfur contents are extremely low in the sediments (up to 0.02 wt% S) and slightly more elevated in the xenoliths (up to 0.6 wt% S).

Among the major elements, carbonate sediment samples demonstrate an enrichment in calcium (11.9–55 wt% CaO), whereas these rocks are variably depleted in all other major elements: SiO_2 (0.2–46.4 wt%), Al_2O_3 (0.1–12 wt%), MgO (0.3–2.2 wt%), and alkalis (up to 0.02–1.0 wt% Na_2O). Compared to the sediment samples, the calc–silicate xenoliths have higher SiO_2 (48–82 wt%, Figure 1); overlapping Al_2O_3 (0.6–16 wt%), Fe_2O_3 (1.7–11.3 wt%), MgO (0.4–5.8 wt%), alkalis (0.05–2.1 wt% Na_2O and 0.02–0.8 wt% K_2O), TiO_2 (0.03–0.6 wt%), and P_2O_5 (up to 0.2 wt%); and lower CO_2 (up to 1.2 wt%) contents. High SiO_2 and Al_2O_3 contents in the xenoliths (MXCS-4: up to 82 wt% SiO_2 and up to 12.45 wt% Al_2O_3) reflect strong enrichment in silicates due to skarn formation (Burt, 1982).

Javanese sediment samples have higher strontium (122–338 ppm) concentrations compared to other trace elements (2.0–63 ppm V) in these samples. The calc–silicate xenoliths are variably enriched in such trace elements as La (1.8–16.4 ppm), Ce (5–32.4 ppm), Co (up to 119 ppm), Cr (up to 674 ppm), Cu (up to 245 ppm), Ba (up to 326 ppm), Sr (154–682 ppm), Zn (20–113 ppm), and Zr (up to 298 ppm) compared to the sediments.

Figure 1 illustrates that sediments have radiogenic strontium isotope signatures ($^{87}Sr/^{86}Sr$ = 0.70684–0.70879) and low $^{143}Nd/^{144}Nd$ isotope ratios (0.51238–0.51254). The xenolith samples are represented by extremely variable Sr isotope ratios (0.70595–0.70938), whereas the Nd isotope ratio range is more modest, from 0.51250 to 0.51278. Pb isotope ratios are variable: $^{206}Pb/^{204}Pb$ (18.491–18.664), $^{207}Pb/^{204}Pb$ (15.524–15.618), and $^{208}Pb/^{204}Pb$ (38.676–38.972).

Micro-textures, minerals, and glasses in the 1994–2010 calc–silicate xenolith samples

1994 xenolith M94-CS-104 (core)

Figure 2A demonstrates that the investigated sample fragment contains one predominant mineral phase: porous wollastonite. It is important to note that the sample also contains accessory calcite with ≤0.1 wt% MnO, larnite (Larn, Ca_2SiO_4), and srebrodolskite (Srbr, $Ca_2Fe^{3+}{}_2O_5$) (Table 3) in the localized zone of the xenolith edge. In the contact zone between the calcite and wollastonite, the sample contains micro-veins and micro-agglomerates (Figure 2A) of porous calcic glasses (31.7 ± 6.8 wt% SiO_2; 37.8 ± 3.1 wt% CaO).

1998 xenolith MXCS1 (rim)

Figures 2B, D represent the edge zone of the xenolith fragment in contact with the lava. This contact zone contains idiomorphic diopside crystals (Table 3) in association with highly silicic glasses (76.5 ± 3.5 wt% SiO_2) with variable low CaO (4.3 ± 2.2 wt %), low alkalis (2.6 ± 0.4 wt% Na_2O and 3.1 ± 0.7 wt% K_2O), and low MgO (up to 1.3 wt%), FeO (1.8 ± 0.8 wt%), and TiO_2 (0.2 ± 0.1 wt%) contents. These natural silicic glasses are richer in SiO_2 and poorer in Cl contents compared to the 2010 Crustal Assimilant and the groundmass 2006 and 2010 Merapi glasses (Figure 4). The notation of the 2010 Crustal Assimilant (natural high-Ca glasses in the 2010 Merapi pyroclastic lava products) has been introduced to describe a model assimilant composition that interacted with the 2010 Merapi pre-eruptive magma based on the work of Borisova et al. (2013), whereas these natural melts have compositions close to those of the partial melts modeled by MELTS. The natural silicic glasses highly enriched in SiO_2 resemble not only those generated by MELTS during the calc–silicate wallrock partial melting (Supplementary Dataset S1) but also those generated by quartz dissolution in the 1991 Pinatubo basaltic xenoliths (Borisova et al., 2014).

1998 xenolith MXCS4 (core)

The investigated xenolith core contains an assemblage of re-crystallized coarse quartz, anorthite, clinopyroxene, and titanomagnetite identified by using a scanning electron microscope (EDS). The anorthite grains are polyhedral with ~120 dihedral angles or porphyroblastic with abundant inclusions (i.e., typical metamorphic textures). Glass was not detected.

2006 xenolith MXCS06KAT2 (rim)

Another xenolith–lava contact zone is represented by the Merapi calc–silicate xenolith from the 2006 BAF (Figure 2C). It is noticed that the contact zone contains xenomorphic crystals of wollastonite ($Wo_{83-97}En_{0-3}$) with up to 0.3 wt% of Al_2O_3 in the groundmass and clusters of euhedral–subhedral individual crystals in highly silicic glass (SiO_2 = 75.2 ± 1.1 wt%, Al_2O_3 = 12.7 ± 0.5 wt%, CaO = 1.7 ± 0.6 wt%, Figure 4). Supplementary Figures A1, A2 demonstrate idiomorphic rims of strongly zoned calcic pyroxenes (CaPx, Wo_{54-82} En_{2-21}) with compositions (Al_2O_3 0.3–2.0 wt%, Mg# = 13–47) intermediate between hedenbergite and wollastonite at the rims. Moreover, at the xenolith–lava contact, the pyroxene cores are Al-poor augite (Wo_{43} En_{42}, Al_2O_3 = 2.3 wt%) and diopside (Wo_{46} En_{46}, Al_2O_3 = 2.1 wt%) that have high Mg# = 74–76.

2010 xenolith 014-1 B (rim)

Figures 2E–H show that the investigated 2010 Merapi xenolith contains wollastonite associated with silicic glasses and an assemblage of re-crystallized anorthite and diopside clinopyroxene as well as titanomagnetite identified by electron microprobe mapping (EPMA). The anorthite grains are polyhedral with ~120 dihedral angles or porphyroblastic

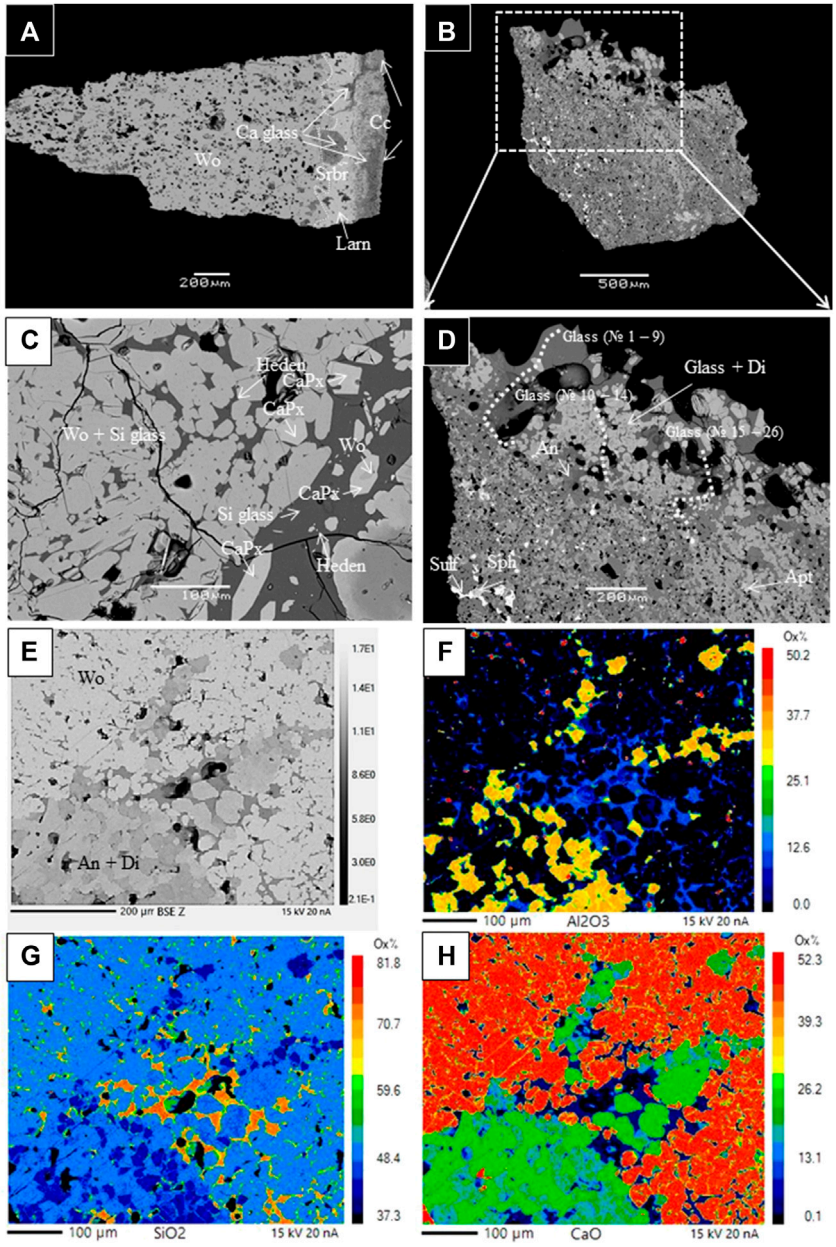

FIGURE 2
Representative backscattered electron images of the 1994–2006 Merapi calc–silicate xenoliths with mineral and glasses phases identified by EDS energy-dispersive X-ray spectroscopy and EPMA. Cc, calcite; Wo, wollastonite; Larn, larnite; Srbr, srebrodolskite; Ca glass, calcic glass; Si glass, silicic glass; Di, diopside, Heden, hedenbergite; An, anorthite; Sulf, sulfide; Sph, sphene; and Apt, apatite. **(A)** M94 CS104 (1994); **(B, D)** MXCS1 (1998); **(C)** MXC06KAT2 (2006); and **(E–H)** 014-1 B (2010).

(i.e., typical metamorphic textures). The presence of silicic glass, detected in an assemblage with massive wollastonite at the rim of the calc–silicate xenolith, suggests production of silica-rich glasses at contact zones between the xenolith and magma.

Partial melt compositions predicted by rhyolite-MELTS modeling

Equilibrium partial melting results using rhyolite-MELTS (version 1.2.0) for two contrasting compositions (SiO_2-rich and CaO-rich, Supplementary Dataset S1 and Table 4) of the calc–silicate xenoliths as the wallrocks from the 1998–2010 Merapi collection (MXCS-1R; MXCS-4, Table 2) are presented in Figure 3 (starting composition) and Figure 4 (modeled partial melt compositions). The SiO_2-rich calc–silicate xenolith, MXCS-4, has a solidus assemblage (~625°C at 200 MPa) of quartz >> garnet >> clinopyroxene > minor feldspar, sphene, and apatite. At its solidus, the assemblage is H_2O-fluid saturated. During partial melting, melts range from ~67 wt% SiO_2 and 12 wt % CaO [at smaller degrees of melt (<1%)] to ~84% SiO_2 at the liquidus. Enriched CaO (>20 wt%) is produced during

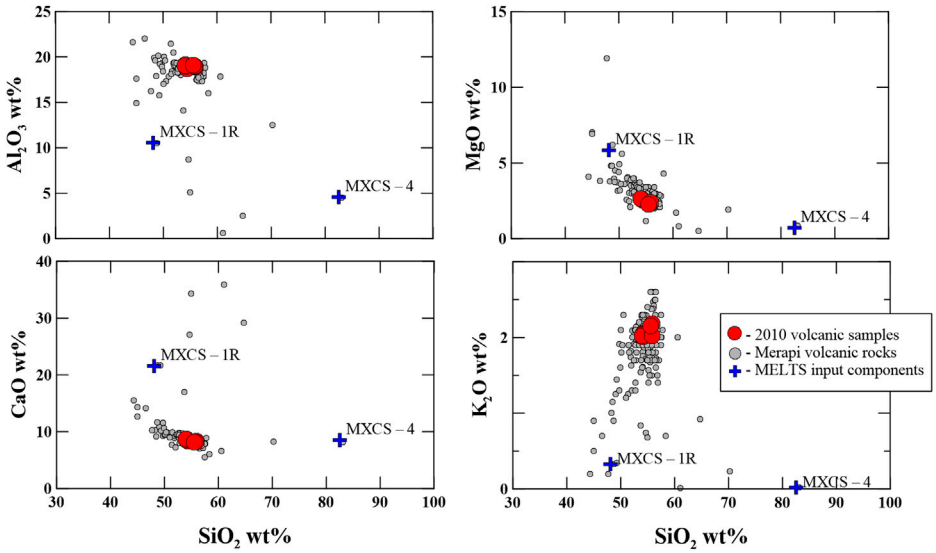

FIGURE 3
The 2010 and other Merapi volcanic rocks and the input component composition used for the thermodynamic modeling of the calc–silicate xenolith partial melting. All details of the thermodynamic modeling (MELTS) are summarized in Table 4 and Supplementary Dataset S1. The Merapi volcanic rocks are from the MERAPIDATA database (Borisova et al., 2011).

equilibrium partial melting between ~790°C (~3.5% partial melt) to ~955°C (25% partial melt). Minerals are consumed in the following order: alkali feldspar (~Or_{80}) at ~630°C, the fluid phase at ~650°C, and apatite and garnet between ~815°C and 845°C, followed by sphene (~950°C), plagioclase (~1055°C), and clinopyroxene (~1100°C). Quartz remains the only solid phase above this temperature to the liquidus. See Figure 4 and Supplementary Dataset S1 for more details.

The CaO-rich xenolith, MXCS-1R, is at ~5% melt at ~656°C, where the rhyolite-MELTS run encountered a quadratic error. The conditions of partial melting are well represented by the rhyolite-MELTS results, despite this. The near-solidus assemblage includes clinopyroxene >> garnet > plagioclase > quartz > minor sphene, alkali feldspar, and apatite. This xenolith is not fluid saturated at any point at 200 MPa. During partial melting, SiO_2 (wt%) values initiate at ~67.9 (~656°C), increase to a maximum of 72.6 (~766°C), and then, decrease to ~51.7 at the liquidus. CaO (wt%) starts at ~11 at 656°C, increases to a maximum of 25.6 at 886°C (~21% melting), and then, decreases to ~23 wt% at the liquidus. Minerals are consumed in the following order: alkali feldspar (~666°C), quartz (~766°C), sphene and garnet between 856°C and 881°C, apatite (~906°C), and plagioclase (1201°C). Clinopyroxene remains the only phase present to the liquidus. See Figure 4 and Supplementary Dataset S1 for more details.

Discussion

Reaction to produce the calc–silicate crust

Figure 2A demonstrates that the investigated sample fragment, 1994 xenolith M94-CS-104, contains one predominant mineral phase: porous wollastonite formed by regular skarn reaction:

$$CaCO_3^S + SiO_2^F = CaSiO_3^S + CO_2^F, \quad (1)$$

where $CaCO_3^S$ is a calcite molecule, SiO_2^F is SiO_2 dissolved in a (an aqueous) fluid (F), $CaSiO_3^S$ is the formed wollastonite mineral, and CO_2^F is the fluid liberated upon reaction. This reaction, also summarized in Figure 5, demonstrates an important flux of silica by shallow aqueous fluid to produce the calc–silicate crust that is enriched in silica relative to the sediments.

Geochemical and mineral tracers of calc–silicate xenolith assimilation

Figure 1 shows that Sr is a unique isotopic tracer of calc–silicate assimilation, whereas Pb isotopes are depleted in the calc–silicate xenoliths compared to the Merapi volcanic rocks. Nd behaves differently depending on the type of the crustal material. As to Sr–Pb isotope signatures, radiogenic Sr and unradiogenic Pb are characteristic features of the Merapi calc–silicate xenoliths (Figure 1). Table 2 also demonstrates that in addition to Sr (up to 682 ppm), trace elements such as Ba (up to 326 ppm), Co (up to 119 ppm), Cr (up to 674 ppm), Cu (up to 245 ppm), V (up to 139 ppm), Zn (up to 105 ppm), and Zr (up to 298 ppm) may be considered as geochemical tracers of calc–silicate crust assimilation. Moderate to strong enrichment of the calc–silicate xenoliths in the trace elements compared to the sediments is likely to be related to aqueous-carbonic fluid reaction at contact metamorphic conditions (Figure 1).

In addition to high Sr contents and radiogenic $^{87}Sr/^{86}Sr$, elevated CO_2, Ba, Co, Cr, Cu, V, Zn, and Zr contents in the magmatic minerals and associated glasses and re-crystallization/dissolution of wallrock sphene, quartz, garnet, apatite, and ilmenite are predicted

TABLE 4 Composition of calc–silicate wallrocks used for rhyolite-MELTS modeling (or MCS modeling).

Component (MCS models[a])	Input data	Ref	SiO2, wt%	TiO2	Al2O3	Fe2O3tot	FeOtot	FeO[b]	Fe2O3[b]	MgO	MnO	CaO	Na2O	K2O	P2O5	H2O	CO2
WR (M1–M5 M10–M11)	MXCS–4[s]	C2007	82.49	0.48	4.55	2.75	-	1.02	0.24	0.72	0.11	8.52	0.16	0.02	0.05	0.07	0.17
WR (M6–M9)	MXCS–1R[s]	C2007	48.11	0.50	10.52	11.31	-	4.18	1.00	5.84	0.32	21.56	0.54	0.33	0.17	0.36	-

All details on the calc–silicate xenoliths MXCS 4 and MXCS 1R may be found in the study of Chadwick et al. (2007).
[a]MCS models according to the study of Borisova et al. (2013; 2016).
[b]FeO and Fe2O3 contents are calculated from either FeOtot or Fe2O3tot contents suggesting FeO/Fe2O3 = 0.24.

by thermodynamic modeling (upon the wallrock melting) and are, thus, important tracers of calc–silicate crust assimilation.

Kinetics of reaction between calc–silicate crust and the Merapi magma

The 1994–2010 Merapi calc–silicate xenoliths are enriched in wollastonite in the core zones and frequently contain calcite as a relic mineral phase (Figure 2A; Deegan et al., 2010). In contrast, the xenoliths' rims are depleted in wollastonite and are commonly enriched in anorthite and diopside. The xenolith samples also contain veins and spherical agglomerates of calcic glasses (31.7 ± 6.8 wt% SiO_2, 37.8 ± 3.1 wt% CaO) (Table 3). This type of natural calcic glass strongly resembles "Ca-rich glasses" (28–38 wt% SiO_2, 27–34 wt% CaO) experimentally produced by Jolis et al. (2013), Deegan et al. (2010), and Blythe et al. (2015) from calcite-enriched material heated with silicate melt at 500 MPa and 1200°C. Moreover, Deegan et al. (2010) reported even more Ca-rich glasses (containing up to 62 wt% CaO) associated with natural wollastonite–calcite in the Merapi xenoliths. We interpret the natural calcic glasses reported in Table 3 to be the result of the reaction between calcite $CaCO_3^S$ and $SiO_2^{L/F}$ (see Eq. 2; Blythe et al., 2015) rather than the "dissociation" proposed by Deegan et al. (2010). Figure 2A demonstrates the occurrence of calcic glasses in the M94 CS104 xenolith in an assemblage with larnite and wollastonite, whereas the major element composition of the calcic glasses coincides with a calcite–quartz control line, suggesting that the composition of the calcic melt is controlled by the following dissolution reaction:

$$CaCO_3^S + SiO_2^{L/F} = CaSiO_3^L + CO_2^F, \quad (2)$$

where $SiO_2^{L/F}$ (silicate melt (L) or fluid (F) form of SiO_2) is derived from the magma, F is fluid, and L is the produced Ca–Si-melt.

In the xenolith rim of MXCS1, the observed assemblage of euhedral–subhedral individual crystals of diopside with highly silicic glasses (76.5 ± 3.5 wt% SiO_2, 12.3 ± 3.2 wt% Al_2O_3, 4.3 ± 2.2 wt% CaO) in the 1998 calc–silicate xenoliths (Table 3; Figure 2B) resembles an association of idiomorphic clinopyroxene rims with silicic glasses around quartz xenocrysts produced by dissolution of quartz phenocrysts during the reaction with basaltic magma (Donaldson, 1986; Borisova et al., 2014). We infer, therefore, that the assemblage of silicic glasses and euhedral–subhedral individual crystals of diopside is the result of incongruent dissolution of metamorphic minerals associated with crystallization of calcic clinopyroxenes in the produced highly silicic melts. The incongruent dissolution reaction may be described as follows:

$$CaSiO_3^S + SiO_2^{L1/S} + MgO^{L1} = CaMgSi_2O_6^S, \quad (3)$$

where $CaSiO_3^S$ is residual wollastonite, SiO_2^{L1} is SiO_2 in the initial melt or solid SiO_2^S quartz, MgO^{L1} is MgO components in the initial melt (L_1), and $CaMgSi_2O_6^S$ is diopside in the produced highly silicic melt. The mechanism of the crustal assimilation may be first marked by incongruent dissolution of crustal metamorphic minerals with generation of highly silicic (77 ± 4 wt% of SiO_2, 12 ± 3 wt% of Al_2O_3) melts in association with idiomorphic diopside [$Wo_{49}En_{29}$; 57 ± 3 Mg# = Mg/(Mg+Fe^{2+})] or other calcic pyroxenes (Wo_{54-82} En_{2-21}; 16–43 Mg#).

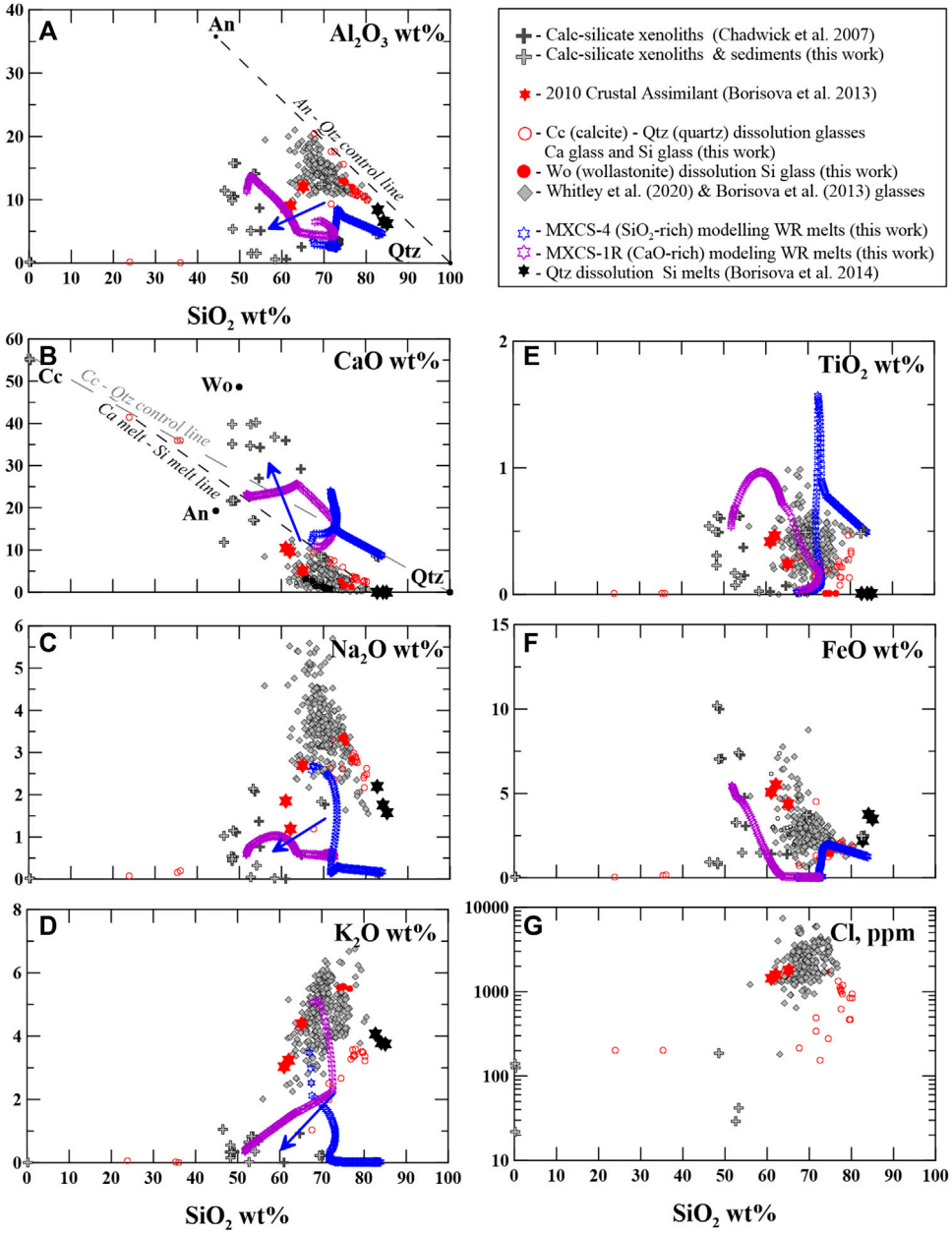

FIGURE 4
(A) Al_2O_3–SiO_2, **(B)** CaO–SiO_2, **(C)** Na_2O–SiO_2, **(D)** K_2O–SiO_2, **(E)** TiO_2–SiO_2, **(F)** FeO–SiO_2, and **(G)** Cl (ppm–SiO_2 (wt%) plotted for the bulk-rock calc–silicate xenoliths and local carbonate sediments, 2006 and 2010 glasses (groundmass), the 2010 Crustal Assimilant glasses compared to the Ca and Si glasses generated by dissolution of calcite, and quartz generated by Woll dissolution. Quartz dissolution glass compositions are from the study of Borisova et al. (2014). The 2006 data are from the study of Costa et al. (2013), and the 2010 data are from the study of Borisova et al. (2013). The MELTS (or MCS) modeling data (see Supplementary Dataset S1) are given for the wallrock melts. The blue arrows indicate the wallrock melt composition trajectories upon the xenolith heating and partial melting (WR). The blue arrows reflect the trends described by the 2010 Crustal Assimilant. An - anorthite; Qtz - quartz; Cc - calcite; Wo - wollastonite.

The highly silicic glasses (melts) may be directly predicted by thermodynamic equilibrium or modeling of partial melting of the calc–silicate xenoliths. The thermodynamic modeling results record silicic melt compositions with the highest SiO_2 = 67–84 wt% and variable CaO = 12–26 wt% contents upon partial melting of the crustal xenoliths due to quartz, garnet, and feldspar consumption. Figure 4 demonstrates that all oxide contents in the modeled highly silicic melts produced at thermodynamic equilibrium during partial melting of calc–silicate xenoliths (at 630°C–1200°C) closely resemble those of the analyzed silicic glasses in the 1994–2010 xenoliths.

Consequently, SiO_2, Al_2O_3, and CaO contents in the generated melts may be controlled by chemical mixing between the silicic melts and generated highly mobile carbonate (Ca-rich) melt. The capacity of carbonate melt rich in CO_3 to be extremely mobile and to migrate from skarns to a

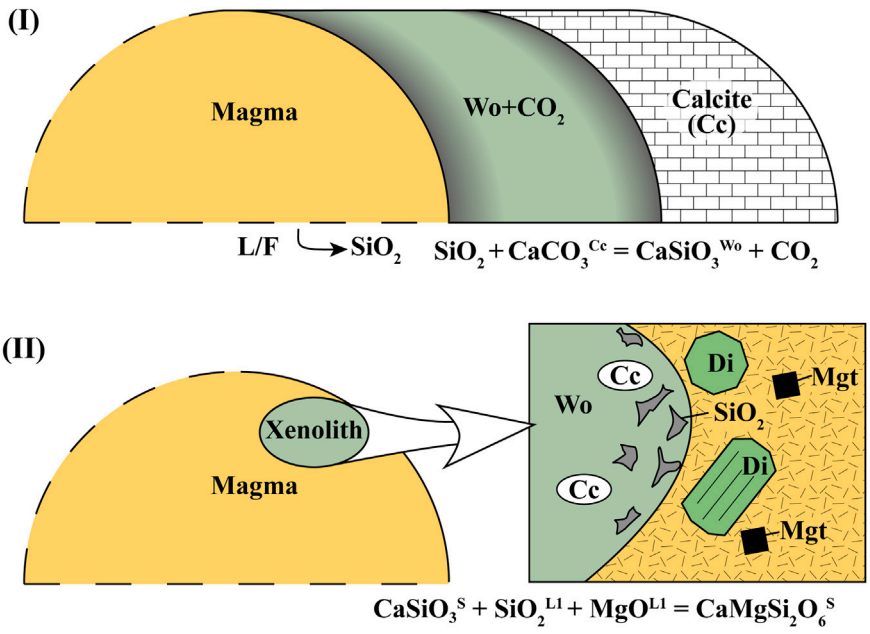

FIGURE 5
Principal schema of (I) the calc–silicate crust production and (II) calc–silicate crust assimilation by the Merapi magma (Merapi volcano, Indonesia). The elevated trace element (Ba, Co, Cr, Cu, V, Zn, and Zr) contents in the calc–silicate crust and the contaminated magma are related to the important flux of these elements from the magmatic source (in form of an aqueous-carbonic fluid) at stage I. Cc, calcite; Wo, wollastonite; Di, diopside; SiO_2, silicic glasses; and Mgt, magnetite. Our hypothesis is that the rate-limiting process is the mixing of the produced crustal melts with andesitic melt (average 65 wt% SiO_2) through chemical diffusion of Si–Al in hybrid aluminosilicate melts.

magma chamber (Gaeta et al., 2009) indicates that CaO-SiO_2-Al_2O_3 contents in the analyzed silicic glasses (Figure 4) can be modeled by mixing between the highly silicic and carbonate melts. In order to explain Al_2O_3 and other major element contents in the assimilating melts (e.g., the 2010 Crustal Assimilant), it is necessary to suggest involvement and chemical mixing with K–Cl-rich andesitic melts (average 65 wt % SiO_2), proposed by Borisova et al. (2013; 2016) as a natural melt component of the resident magma. We hypothesize that the rate limiting process of the crustal assimilation is the mixing of the produced crustal melts with the andesitic to basaltic andesite melts through Si–Al diffusion that explains major and volatile (Cl) element contents in the Merapi glass products.

Physical–chemical disequilibrium *versus* thermodynamic modeling

We predict that because of rapid heat diffusion, the calc–silicate material has to reach the temperature of 900°C rapidly upon the magma–xenolith interaction, suggesting effective partial melting and dissolution of the crustal xenoliths at 900°C. Thermal stability of carbonates is limited to a temperature range of 820°C–870°C (Ar and Doğu, 2001). Calcite starts to decompose at 620°C, and the calcination reaction is completed at 820°C at atmospheric pressure (Stern & Weise, 1966; Ar and Doğu, 2001), suggesting complete consumption of calcite at the pre-eruptive temperatures of 925°C–1100°C. Given the chemical equilibrium during contact metamorphism created by heat flow from basaltic andesite magma, the xenolith (several cm in size) should attain the pre-eruptive temperature of 925°C–1100°C at 200–300 MPa. Nevertheless, the calcite inclusions (Deegan et al., 2010; Borisova et al., 2013) and calcite–larnite–wollastonite assemblage (Figure 2) are observed in the Merapi calc–silicate xenoliths as metastable mineral phases.

These observations suggest that the reaction between the magma and the 1994–2010 calc–silicate xenoliths was out of physical–chemical (or thermodynamic) equilibrium. The disequilibrium may be related to sluggish kinetics of the residual calcite consumption and Si–Al diffusion in the hybrid melt. In any case, it is likely that the crust–magma interaction is controlled by kinetics of reactions such as crustal partial melting, mineral dissolution and recrystallization, and melt mixing. Nevertheless, the mechanism of crustal calc–silicate material assimilation can be well predicted by thermodynamic modeling using rhyolite-MELTS, whereas more experiments are required to constrain the rate of the calc–silicate material-silicate magma interactions. Based on available experimental data (Zhang et al., 1989; Shaw, 2006), we predict that this crustal assimilation rate is controlled by Si–Al diffusion in the hydrous silicic melts produced during the melt–crust interaction. These experimental data suggest that silica activity in the melt defines the maximal dissolution rate, whereas the melt viscosity determines whether this maximum rate may be achieved in the case of diffusion control.

Conclusion

1) *In situ* electron probe microanalyses of the 1994–2010 calc–silicate xenolith minerals and glasses and the observed reactions and thermodynamic modeling using MELTS or MCS suggest that selective assimilation at ~ 650°C–1100°C and 200–300 MPa prior to the 1994–2010 eruptions preserved wollastonite and carbonate melts quenched to natural calcic glasses (32 ± 7 wt% SiO_2, 38 ± 3 wt % CaO) as well as minor calcite mineral as a thermodynamically metastable mineral phases in the calc–silicate xenoliths. The following reaction happened during the 1994–2010 calc–silicate xenolith interaction with the Merapi magma:

$CaSiO_3^S + SiO_2^{L1/S} + MgO^{L1} = CaMgSi_2O_6^S$, where $CaSiO_3^S$ is residual metastable wollastonite, $SiO_2^{L1/S}$ are SiO_2 and MgO in the initial melt (L_1) or quartz (S), MgO^{L1} is MgO in the initial melt (L_1), and $CaMgSi_2O_6^S$ is diopside in the produced highly silicic melt.

2) The mechanism of the 1994–2010 calc–silicate xenolith assimilation is generation of highly silicic (77 ± 4 wt% of SiO_2, 12 ± 3 wt% of Al_2O_3) melts in association with idiomorphic diopside [$Wo_{49}En_{29}$; 57 ± 3 Mg# = Mg/(Mg+Fe^{2+})] or other calcic pyroxenes (Wo_{54-82} En_{2-21}; 16–43 Mg#) due to mineral dissolution and recrystallization reactions. Modeling using rhyolite-MELTS predicts that the major element composition of the generated silicic glasses (up to 67–84 wt % SiO_2) is controlled by the calc–silicate material partial melting.
3) In addition to elevated Sr contents and radiogenic $^{87}Sr/^{86}Sr$ ratio, important geochemical tracers of the calc–silicate assimilation are elevated CO_2, Ba, Co, Cr, Cu, V, Zn, and Zr contents in the minerals and glasses. The re-crystallization/dissolution of wallrock-derived sphene, quartz, garnet, apatite, and ilmenite is predicted by thermodynamic modeling (upon the wallrock partial melting) and, thus, are important mineral tracers of crustal assimilation.
4) Although kinetics of the calc–silicate material–melt interaction likely control the calc–silicate assimilation process, the mechanism of the assimilation process can be well predicted by thermodynamic modeling (MELTS or MCS). Further application of kinetic experiments on the calc–silicate material interaction with aluminosilicate magma is useful to quantify the rates of crustal assimilation. We hypothesize that the rate-limiting process of crustal assimilation is chemical mixing of the produced crustal melts through the chemical diffusion of Si–Al in hybrid melts associated with convection.

Data availability statement

The original contributions presented in the study are included in the article/Supplementary Material; further inquiries can be directed to the corresponding author.

Author contributions

All authors listed have made a substantial, direct, and intellectual contribution to the work and approved it for publication.

Funding

This study was supported by the VELI national site "Volcans Explosifs Laboratoire Indonesien" and the mixed laboratory "Indonesian Subduction and associated risks" or "Subductions Indonésiennes et Risques associés" (SIR) in France and US National Science Foundation projects 1551052 and 2151038.

Acknowledgments

The authors thank the editor Patrizia Fiannacca, S. Erdmann, and another reviewer for the important suggestions on this work, Valentin R. Troll and Frances Deegan for providing the 1998—2006 Merapi xenolith and sediment samples, and Philippe de Parseval for electron probe mapping of the 2010 Merapi sample. The 2015 French expedition provided the 2006–2010 Merapi products for this work.

Conflict of interest

The authors declare that the research was conducted in the absence of any commercial or financial relationships that could be construed as a potential conflict of interest.

Publisher's note

Supplementary material

The Supplementary Material for this article can be found online at: https://www.frontiersin.org/articles/10.3389/feart.2023.1186207/full#supplementary-material

References

Ar, I., and Doğu, G. (2001). Calcination kinetics of high purity limestones. *Chem. Engeneering J.* 83, 131–137. doi:10.1016/s1385-8947(00)00258-8

Blythe, L. S., Deegan, F. M., Freda, C., Jolis, E. M., Masotta, M., Misiti, V., et al. (2015). CO_2 bubble generation and migration during magma – carbonate interaction. *Contrib. Mineral. Petrol.* 169, 42. doi:10.1007/s00410-015-1137-4

Bohrson, W. A., Spera, F. J., Ghiorso, M. S., Brown, G. A., Creamer, J., and Mayfield, A. (2014). Thermodynamic model for energy-constrained open-system evolution of crustal magma bodies undergoing simultaneous recharge, assimilation and crystallization: the magma chamber simulator. *J. Petrology* 55, 1685–1717. doi:10.1093/petrology/egu036

Bohrson, W. A., Spera, F. J., Heinonen, J. S., Brown, G. A., Scruggs, M. A., Adams, J. V., et al. (2020). Diagnosing open-system magmatic processes using the magma chamber simulator (MCS): part I—major elements and phase equilibria. *Contributions Mineralogy Petrology* 175, 104–129. doi:10.1007/s00410-020-01722-z

Borisova, A. Y., Gurenko, A. A., Martel, C., Kouzmanov, K., Cathala, A., Bohrson, W. A., et al. (2016). Oxygen isotope heterogeneity of arc magma recorded in plagioclase from the 2010 Merapi eruption (Central Java, Indonesia). *Geochimica Cosmochimica Acta* 190, 13–34. doi:10.1016/j.gca.2016.06.020

Borisova, A. Y., Martel, C., Gouy, S., Pratomo, I., Sumarti, S., Toutain, J-P., et al. (2013). Highly explosive 2010 Merapi eruption: evidence for shallow-level crustal assimilation and hybrid fluid. *J. Volcanol. Geotherm. Res.* 261, 193–208. doi:10.1016/j.jvolgeores.2012.11.002

Borisova, A. Y., Martel, C., Pratomo, I., Toutain, J., Sumarti, S., and Surono, S. "Merapidata: new petrologic and geochemical database of the Merapi volcano, central java, Indonesia," in Proceedings of the AGU Fall Meeting Abstracts, San Francisco, California, December 2011, V21E–V2536.

Borisova, A. Y., Pichavant, M., Bény, J.-M., Rouer, O., and Pronost, J. (2005). Constraints on dacite magma degassing and regime of the June 15, 1991, climactic eruption of Mount Pinatubo (Philippines): new data on melt and crystal inclusions in quartz. *J. Volcanol. Geotherm. Res.* 145 (1-2), 35–67. doi:10.1016/j.jvolgeores.2005.01.004

Borisova, A. Y., Pokrovski, G. S., Pichavant, M., Fréydier, R., and Candaudap, F. (2010). Amorphous Materials: properties, Structure, and Durability: arsenic enrichment in hydrous peraluminous melts: insights from femtosecond laser ablation-inductively coupled plasma-quadrupole mass spectrometry, and *in situ* X-ray absorption fine structure spectroscopy. *Am. Mineralogist* 95, 1095–1104. doi:10.2138/am.2010.3424

Borisova, A. Y., Toutain, J-P., Dubessy, J., Pallister, J., Zwick, A., and Salvi, S. (2014). H2O–CO2–S fluid triggering the 1991 Mount Pinatubo climactic eruption (Philippines). *Bull. Volcanol.* 76, 800. doi:10.1007/s00445-014-0800-3

Borisova, A. Y., Toutain, J-P., Stefansson, A., Gouy, S., and de Parseval, Ph. (2012). Processes controlling the 2010 Eyjafjallajökull explosive eruption. *J. Geophys. Res. Solid Earth* 117, B5. doi:10.1029/2012JB009213

Burt, D. M. (1982). Skarn deposits; historical bibliography through 1970. *Econ. Geol.* 77 (4), 755–763. doi:10.2113/gsecongeo.77.4.755

Carignan, J., Hild, P., Mevelle, G., Morel, J., and Yeghicheyan, D. (2001). Routine analyses of trace elements in geological samples using flow injection and low pressure on-line liquid chromatography coupled to icpms: A study of geochemical reference materials br, DR-N, UB-N, AN-G and gh. *Geostand. Geoanal. Res.* 25, 187–198. doi:10.1111/j.1751-908X.2001.tb00595.x

Chadwick, J. P. (2008). "Crustal processes in volcanic systems: case studies from northern Ireland, New Zealand and Indonesia,". Ph.D. Thesis (Dublin, Ireland: University of Dublin), 274.

Chadwick, J. P., Troll, V. R., Ginibre, C., Morgan, D., Gertisser, R., Waight, T. E., et al. (2007). Carbonate assimilation at Merapi volcano, java, Indonesia: insights from crystal isotope stratigraphy. *J. Petrology* 48, 1793–1812. doi:10.1093/petrology/egm038

Cloquet, C., Carignan, J., and Libourel, G. (2006). Atmospheric pollutant dispersion around an urban area using trace metal concentrations and Pb isotopic compositions in epiphytic lichens. *Atmos. Environ.* 40, 574–587. doi:10.1016/j.atmosenv.2005.09.073

Costa, F., Andreastuti, S., Bouvet de Maisonneuve, C., and Pallister, J. (2013). Petrological insights into the storage conditions, and magmatic processes that yielded the centennial 2010 Merapi explosive eruption. *J. Volcanol. Geotherm. Res.* 261, 209–235. doi:10.1016/j.jvolgeores.2012.12.025

Deegan, F. M., Troll, V. R., Freda, C., Misiti, V., Chadwick, J. P., McLeod, C. L., et al. (2010). Magma–carbonate interaction processes and associated CO_2 release atMerapi volcano, Indonesia: insights from experimental petrology. *J. Petrology* 51, 1027–1051. doi:10.1093/petrology/egq010

Deegan, F. M., Troll, V. R., Gertisser, R., and Freda, C. (2023). "Magma-carbonate interaction at Merapi volcano, Indonesia," in *Merapi Volcano. Active volcanoes of the world*. Editors R. Gertisser, V. R. Troll, T. R. Walter, I. G. M. A. Nandaka, and A. Ratdomopurbo (Cham, Germany: Springer). doi:10.1007/978-3-031-15040-1_10

Erdmann, S., Martel, C., Pichavant, M., Bourdier, J. L., Champallier, R., Komorowski, J. C., et al. (2016). Constraints from phase equilibrium experiments on pre-eruptive storage conditions in mixed magma systems: A case study on crystal-rich basaltic andesites from mount Merapi, Indonesia. *J. Petrology* 57 (3), 535–560. doi:10.1093/petrology/egw019

Erdmann, S., Martel, C., Pichavant, M., and Kushnir, A. (2014). Amphibole as an archivist of magmatic crystallization conditions: problems, potential, and implications for inferring magma storage prior to the paroxysmal 2010 eruption of mount Merapi, Indonesia. *Contributions Mineralogy Petrology* 167, 1016–1023. doi:10.1007/s00410-014-1016-4

Freda, C., Gaeta, M., Misiti, V., Mollo, S., Dolfi, D., and Scarlato, P. (2008). Magma–carbonate interaction: an experimental study on ultrapotassic rocks from alban hills (central Italy). *Lithos* 101, 397–415. doi:10.1016/j.lithos.2007.08.008

Gaeta, M., Di Rocco, T., and Freda, C. (2009). Carbonate assimilation in open magmatic systems: the role of melt-bearing skarns and cumulate-forming processes. *J. Petrology* 50, 361–385. doi:10.1093/petrology/egp002

Ghiorso, M. S., and Gualda, G. A. R. (2015). An H2O-CO2 mixed fluid saturation model compatible with rhyolite-MELTS. *Contributions Mineralogy Petrology* 169, 53. doi:10.1007/s00410-015-1141-8

Gualda, G. A., Ghiorso, M. S., Lemons, R. V., and Carley, T. L. (2012). Rhyolite-MELTS: A modified calibration of MELTS optimized for silica-rich, fluid-bearing magmatic systems. *J. Petrology* 53 (5), 875–890. doi:10.1093/petrology/egr080

Heinonen, J. S., Bohrson, W. A., Spera, F. J., Brown, G. A., Scruggs, M. A., and Adams, J. V. (2020). Diagnosing open-system magmatic processes using the magma chamber simulator (MCS): part II—trace elements and isotopes. *Contributions Mineralogy Petrology* 175, 105–121. doi:10.1007/s00410-020-01718-9

Iacono-Marziano, G., Gaillard, F., and Pichavant, M. (2008). Limestone assimilation by basaltic magmas: an experimental re-assessment and application to Italian volcanoes. *Contributions Mineralogy Petrology* 155, 719–738. doi:10.1007/s00410-007-0267-8

Iacono-Marziano, G., Gaillard, F., Scaillet, B., Pichavant, M., and Chiodini, G. (2009). Role of non-mantle CO_2 in the dynamics of volcano degassing: the mount vesuvius example. *Geology* 37, 319–322. doi:10.1130/g25446a.1

Jarosevich, E., Nelen, J. A., and Norberg, J. A. (1980). Reference samples for electron microprobe analysis. *Geostand. Newsletters* 4, 43–47. doi:10.1111/j.1751-908x.1980.tb00273.x

Jolis, E. M., Freda, C., Troll, V. R., Deegan, F. M., Blythe, L. S., McLeod, C. L., et al. (2013). Experimental simulation of magma-carbonate interaction beneath Mt.Vesuvius, Italy. *Contributions Mineralogy Petrology* 166, 1335–1353. doi:10.1007/s00410-013-0931-0

Jousset, P., Pallister, J., and Surono (2013). The 2010 eruption of Merapi volcano. *J. Volcanol. Geotherm. Res.* 261, 1–6. doi:10.1016/j.jvolgeores.2013.05.008

Luais, B., Telouk, P., and Albarède, F. (1997). Precise and accurate neodymium isotopic measurements by plasma-source mass spectrometry. *Geochim. Cosmochim. Acta* 61, 4847–4854. doi:10.1016/S0016-7037(97).00293-7

Manhès, G., Allegre, C. J., Dupré, B., and Hamelin, B. (1980). Lead isotope study of basic-ultrabasic layered complexes–speculations about the age of the Earth and primitive mantle characteristics. *Earth Planet. Sci. Lett.* 47, 370–382. doi:10.1016/0012-821X(80)90024-2

Mollo, S., Gaeta, M., Freda, C., DiRocco, T., Misiti, V., and Scarlato, P. (2010). Carbonate assimilation in magmas: A reappraisal based on experimental petrology. *Lithos* 114, 503–514. doi:10.1016/j.lithos.2009.10.013

Pichavant, M., Martel, C., Bourdier, J.-L., and Scaillet, B. (2002). Physical conditions, structure, and dynamics of a zoned magma chamber: mount Pelée (Martinique, Lesser Antilles Arc). *J. Geophys. Res.* 107 (B5), 2093. doi:10.1029/2001JB000315

Pin, C., Briot, D., Bassin, C., and Poitrasson, F. (1994). Concomitant separation of strontium and samarium-neodymium for isotopic analysis in silicate samples, based on specific extraction chromatography. *Anal. Chim. Acta* 298, 209–217. doi:10.1016/0003-2670(94)00274-6

Pouchou, J. L., and Pichoir, F. (1984). A new model for quantitative X-ray-microanalysis. Application to the analysis of homogenous samples. *La Rech. Aerosp.* 3, 167–192.

Schwarzkopf, L. M., Schmincke, H. U., and Cronin, S. J. (2005). A conceptual model for block-and-ash flow basal avalanche transport and deposition, based on deposit architecture of 1998 and 1994 Merapi flows. *J. Volcanol. Geotherm. Res.* 139 (1-2), 117–134. doi:10.1016/j.jvolgeores.2004.06.012

Shaw, C. S. J. (2006). Effects of melt viscosity and silica activity on the rate and mechanism of quartz dissolution in melts of the CMAS and CAS systems. *Contrib. Mineral. Petrol.* 151, 665–680. doi:10.1007/s00410-006-0086-3

Smyth, H., Hall, R., Hamilton, J., and Kinny, P. "East Java: cenozoic basins, volcanoes and ancient basement," in Proceedings of the Indonesian Petroleum Association, 30th Annual Convention, Jakarta, Indonesia, January 2005, 251–266.

Stern, K. H., and Weise, E. L. (1966). *High temperature properties and decomposition of inorganic salts: Carbonates*. Maryland, USA: US Department of Commerce, National Bureau of Standards.

Thirlwall, M. F. (2002). Multicollector ICP-MS analysis of Pb isotopes using a 207Pb-204Pb double spike demonstrates up to 400 ppm/amu systematic errors in Tl-normalization. *Chem. Geol.* 184, 255–279. doi:10.1016/S0009-2541(01)00365-5

Troll, V. R., Deegan, F. M., Jolis, E. M., Harris, C., Chadwick, J. P., Gertisser, R., et al. (2013). Magmatic differentiation processes at Merapi volcano: inclusion petrology and oxygen isotopes. *J. Volcanol. Geotherm. Res.* 261, 38–49. doi:10.1016/j.jvolgeores.2012.11.001

Voight, B., Constantine, E. K., Siswowidjoyo, S., and Torley, R. (2000). Historical eruptions of Merapi volcano, central Java, Indonesia, 1768–1998. *J. Volcanol. Geotherm. Res.* 100 (1-4), 69–138. doi:10.1016/s0377-0273(00)00134-7

Whitley, S., Halama, R., Gertisser, R., Preece, K., Deegan, F. M., and Troll, V. R. (2020). Magmatic and metasomatic effects of magma–carbonate interaction recorded in calc-silicate xenoliths from Merapi volcano (Indonesia). *J. Petrology* 61, 1–38. doi:10.1093/petrology/egaa048

Zhang, Y., Walker, D., and Lesher, C. E. (1989). Diffusive crystal dissolution. *Contributions Mineralogy Petrology* 102, 492–513. doi:10.1007/bf00371090